Materials Science & Engineering A 926 (2025) 147951

Contents lists available at ScienceDirect

Materials Science & Engineering A

journal homepage: www.elsevier.com/locate/msea

Dynamics and structure of the B2→B19' phase transformation in NiTi revealed through *in situ* 4D-STEM

Jennifer Donohue [a], Sean H. Mills [a,b], Benjamin H. Savitzky [b], Steven E. Zeltmann [a], Colin Ophus [b], Andrew M. Minor [a,b,*]

[a] Materials Science and Engineering, University of California at Berkeley, Berkeley, CA, USA
[b] National Center for Electron Microscopy, Molecular Foundry, Lawrence Berkeley National Laboratory, Berkeley, CA, USA

ARTICLE INFO

Keywords:
NiTi
Shape memory alloys (SMAs)
Martensitic phase transformation
In situ transmission electron microscopy (TEM)
Four-dimensional scanning electron microscopy (4DSTEM)

ABSTRACT

The structural evolution of NiTi during the B2→B19' martensitic phase transformation via thermal cycling is investigated using *in situ* four dimensional scanning transmission electron microscopy (4D-STEM). With 4D-STEM, we can directly visualize and quantify the nanoscale evolution of the martensitic structure on thermal cycling and also investigate the origin of diffuse scattering of NiTi in the pre-transitional state. Mapping of the martensite orientation and strain visualizes the progression of the transformation front and self-accommodation of the B19' structure. Diffuse streaking and strain are measured in the pre-transitional austenite (B2) phase and demonstrate no localization or preferential directionality hinting that long-range homogeneous instability rather than nanoscale heterogeneities may be the origin of the pre-transitional anomalies in NiTi. Finally, it is revealed that NiTi does not reform the same martensite nanostructure on thermal cycling but does express similar features. This small variation is likely owing to transformation-induced dislocations.

1. Introduction

The martensitic phase transformation in near-equiatomic Nickel Titanium (NiTi) gives rise to two unique behaviors: the shape memory effect (SME) and superelasticity (SE) [1]. These behaviors make NiTi an incredibly important and an attractive functional material finding wide applications in the medical and engineering disciplines [2–5]. However, most of these applications depend critically on the thermoelastic behavior of the NiTi alloy allowing it to reversibly transform back and forth from austenite to martensite [1].

The martensitic transformation is a diffusionless solid-state transformation in which atoms move in a cooperative manner from old to new lattice positions. This transformation in near-equiatomic NiTi from the high-temperature cubic B2 phase to the low-temperature monoclinic B19' phase occurs via anisotropic lattice strain and shear along the $[100]_{B2}$ direction and governs the SME and SE behaviors [1]. However, the deformation of the B2 lattice alone is not enough to provide an invariant plane. To account for this, NiTi forms a combination of multiple habit plane variants and twins to reduce the strain energy during the transition in a process known as self-accommodation [1,6].

While this transformation has been extensively studied [1] since the discovery of the SME in NiTi by Buehler et al. [7,8] in 1963, there are still open questions which only direct visualization of the local nanostructure can fully answer [9]. Herein we will address two such questions: (1) the nanoscale evolution of the martensitic structure on thermal cycling and (2) the origin of diffuse scattering of NiTi in the pre-transitional state.

It is well known that NiTi undergoes significant changes to some critical properties upon thermal and/or mechanical cycling including reduction in the martensitic transformation temperature (M_s), increase in resistivity [10], decreased recoverable strain, and hysteresis reduction [11,12]. The origin of these changes has been associated with energy dissipation via frictional work and plastic accommodation. The former is related to the energy required to overcome the resistance to interfacial motion between the austenite and martensite phases owing to lattice mismatch. The latter is primarily associated with the introduction of dislocations stemming from the coherency strains of the austenite-martensite interface [1,12–14]. Some work even suggests that the cyclic variation in NiTi properties may be the result of dislocation mediated nucleation of the R-phase resulting in a two-step phase transition [1].

Early work [15] on the cyclic behavior of NiTi suggested that the

* Corresponding author. Department of Materials Science and Engineering, University of California Berkeley, 2607 Hearst Ave., Berkeley, CA, 94720, USA.
E-mail address: aminor@berkeley.edu (A.M. Minor).

https://doi.org/10.1016/j.msea.2025.147951
Received 19 June 2024; Received in revised form 27 January 2025; Accepted 27 January 2025
Available online 28 January 2025

material would re-form the exact same martensitic structure upon thermal cycling making the origin of these property changes unclear. However, more recent work has demonstrated that the martensite structure may vary from cycle to cycle [16–18], however these nanoscale variations have not been fully elucidated. In this work we aim to observe the structural evolution of martensite in NiTi on thermal cycling with 4D-STEM.

The second aim of this work is to study the pre-transitional state in NiTi to improve our understanding of the fundamental origin of the martensitic phase transition and the formation of the subsequent martensitic structure. NiTi is considered to be in the pre-transitional state when it is close to but above M_s, usually 10–100 °C above M_s [19]. This pre-transitional state is of particular interest as the material in this condition is considered to have latent instability with respect to the martensitic transition which increases on cooling until finally reaching M_s [1,20]. Anomalous properties including softening of elastic shear constants [21–24], diffuse streaking in electron and X-ray diffraction patterns [1,25], tweed structures observed in transmission electron microscopy (TEM), decrease of sound velocity (ultrasonic attenuation) [2,26], and negative temperature coefficient of electrical resistivity [2] have been observed in the B2 austenite phase in the pre-transitional state of NiTi. Some of these properties have been explained by the discovery of the presence of an intermediate phase, known as the R-phase, in the transition from the high temperature B2 phase to the low temperature B19' phase producing a two-step phase transformation (B2→R→B19'). However, not all of the anomalous properties are explained by this mechanism. In fact, several anomalous properties including softening of the elastic constants and diffuse streaking in diffraction space are present whether the system progresses through a two-step or one-step phase transition [1]. In addition, the presence of residual martensite in the pre-transitional austenite phase potentially dislocation-mediated or nucleated has also been suggested [27,28] to be responsible for some of these anomalous properties. Other explanations for these anomalies include incomplete phonon softening [29] which has been observed in the pre-martensitic B2 lattice and implies the pre-martensitic B2 phase contains information about the incipient transformation which is expressed in these anomalous properties. With this work, we aim to understand the origin of diffuse streaking in electron diffraction patterns in pre-transitional NiTi and assess the presence of predictive nanoscale structures which may contain information about why one martensite structure is favored over another.

For this study we utilize the emerging nanobeam diffraction tool, four-dimensional scanning transmission electron microscopy (4D-STEM). With the advent of high-speed detectors and high-throughput data processing routines [30,31], 4D-STEM has become as a powerful technique for the collection of nanoscale localized structural information over a large sample area providing a wealth of information. The method involves rastering a converged electron nanobeam across a sample producing a two-dimensional diffraction pattern at each scan position [32]. This provides both the high spatial resolution and the diffraction information needed to map the structural evolution of NiTi on thermal cycling. In this paper we describe our *in situ* 4D-STEM study of the phase transformation front on cooling and development of the martensitic structure on cycling in NiTi.

2. Methods

2.1. Materials and processing

For this work, equiatomic NiTi was obtained from NexMetal corporation. The received material was encapsulated in an argon filled quartz tube and homogenized at 1000 °C for 24 h with an oxygen getter. Differential Scanning Calorimetry was performed at 5 °C/min to verify the one-step (B2→B19') phase transformation and calculate the composition of $Ni_{50.15}Ti_{49.85}$ (at. %). The grain size was 50–100 μm after homogenization as observed in S/TEM. Energy Dispersive Spectroscopy (SEM-EDS) and STEM-EDS confirmed no significant second phases were present, and no nanoscale precipitates were observed during the course of these experiments.

TEM samples were prepared via twin-jet polishing according to Pourbabak et al. [33]. Initially, the homogenized material was mechanically polished to a thickness of 40–80 μm. After the mechanical polishing process the sample was thermally cycled through the martensitic phase transition 3 times to melt the crystal bond adhesive used. Electropolishing was performed using an electrolyte solution of 30 % nitric acid and 70 % methanol at 20V at a temperature between −28 °C and −36 °C. Samples were then rinsed in methanol and dried before STEM imaging.

Prior to the *in situ* microscopy experiments, all samples were held at a temperature of at least 180 °C for ≥1h to remove potential carbon contamination. The initial data set demonstrating the transformation front progression was acquired over a ~4h microscope session. The sample was cooled at a rate of ~3 °C/min and held at each scan temperature for at least 10 min to allow for equilibration before 4D-STEM scans were acquired. During the thermal cycling experiment, samples were repeatedly heated to 210 °C and cooled to room temperature (~18 °C). Heating and cooling were done at a rate of ~5 °C/min. The sample was held for ~10 min prior to obtaining 4D-STEM data to allow for thermal equilibration.

2.2. Transmission electron microscopy

Transmission electron microscopy was performed at the National Center for Electron Microscopy in the Molecular Foundry at the Lawrence Berkeley National Laboratory on a Thermo Fisher Scientific TitanX microscope operating at a 300 kV accelerating voltage with "bullseye" apertures for high precision strain measurements [34]. A Gatan 652 double tilt *in situ* heating holder was utilized for this work. The temperature at the sample is difficult to determine precisely and so all temperatures reported correspond to the thermocouple reading built into the holder. The relative changes in temperature reported are considered to be accurate. The 4D-STEM data sets were acquired on the Gatan Orius CCD camera with a 33 ms exposure time. A convergence angle of 0.7 milliradians with a step size of 5 nm was used to acquire the initial data set demonstrating the transformation front progression. A convergence angle of 0.5 milliradians and a step size of 15 nm was used to acquire the 4D-STEM data over the course of multiple cycles.

With the data acquired, Bragg disk detection was performed according to Savitzky et al. [30], using built-in functions of the software package py4DSTEM to reduce the complexity and dimensionality of the 4D-STEM data. Following this, the Bragg peak locations were corrected for diffraction shifts. An aluminum standard was used to calculate diffraction space pixel size and elliptical distortion. With the peaks detected, mapping of the martensite variants was performed using a virtual dark field detectors to integrate the intensity of the superlattice peaks located at $\frac{1}{2}\{011\}_{B2}$ associated with each variant as depicted by the red, green, and blue coloring in Fig. 1. The variants were also mapped by integrating the intensity of the detected Bragg peak at the relevant superlattice positions. Indexing of crystalline orientation was done using built-in functions of py4DSTEM implementing the method introduced by Ophus et al. [31] in 2022. Bragg peaks were indexed to the B19' structure as reported by Kudoh et al. [35] with minor modifications to account for compositional differences. Finally, strain mapping was performed using built in methods of py4DSTEM. Simulated diffraction patterns shown in Fig. 2 and S1 were calculated using py4DSTEM and lattices reported for the R-phase [36,37], B2 austenite phase [1], and B19' monoclinic phase [35].

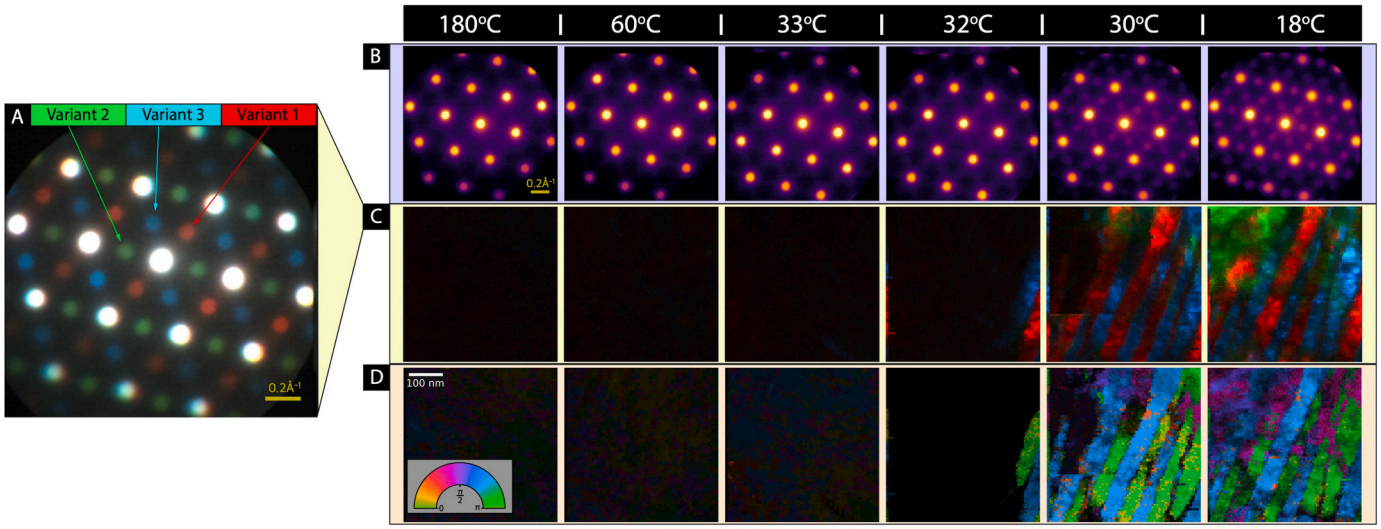

Fig. 1. 4D-STEM based structure identification of austenite to martensite transformation upon cooling. (a) Average diffraction pattern from 4D-STEM acquisition of NiTi at 18 °C along the $[111]_{B2}$ zone axis with red, green, and blue coloration indicating superlattice peaks associated with three martensite variant types mapped in (c) which shows the formation of martensite structures on cooling through the transformation temperature, (b) the average diffraction pattern from the 4D-STEM data set acquired at the indicated temperature, and (d) in-plane rotation of the entire $[-101]_{B19'}$ diffraction pattern demonstrating the orientation relationships between the three variants mapped in (c). (For interpretation of the references to color in this figure legend, the reader is referred to the Web version of this article.)

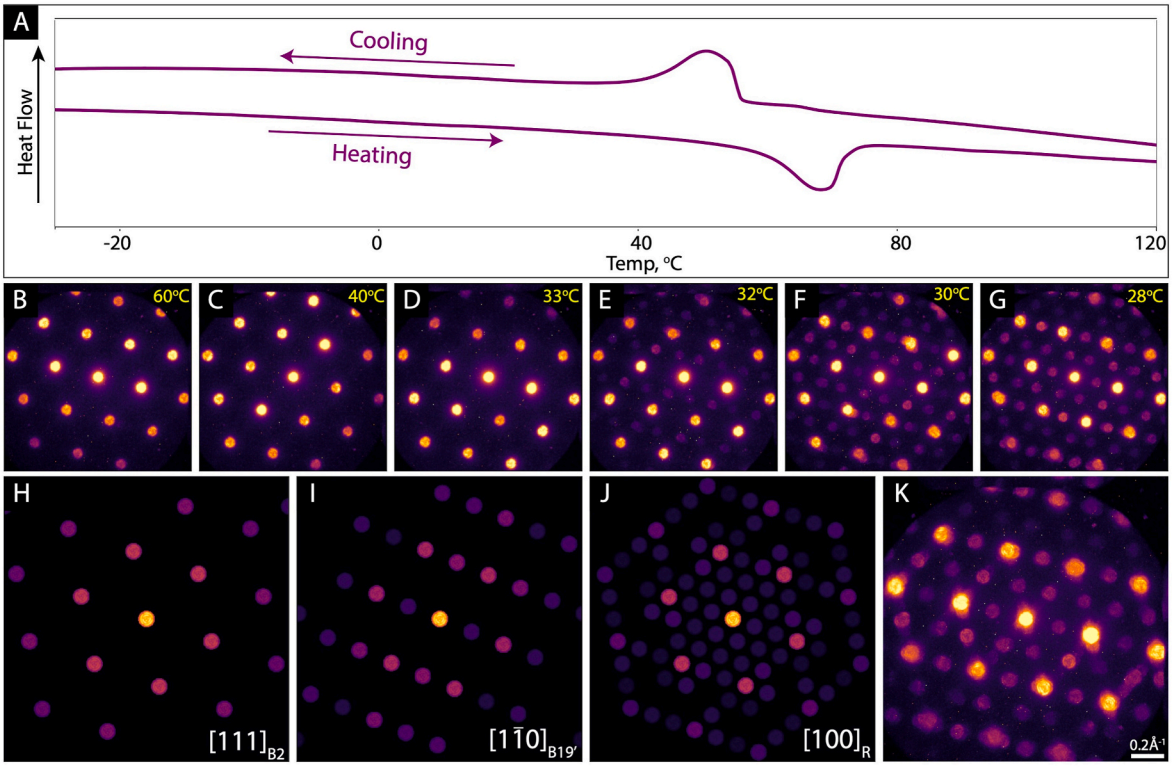

Fig. 2. Representative diffraction patterns through phase transformation. (a) DSC demonstrating a clear one-step phase transition in both the forward and reverse, (b-g, k) show the maximal diffraction pattern from the 4D-STEM data set acquired at each temperature indicated in the top right corner, and (h–j) show simulated electron diffraction patterns for the B2 zone axis in this experiment, the corresponding of zone-axes of the B19', and the R-phase.

3. Results

3.1. Structural mapping of NiTi through the B2→B19' phase transformation

Fig. 1 shows the structure of NiTi upon cooling through the martensitic phase transition as visualized by *in situ* 4D-STEM. Fig. 1b shows the evolution of the average diffraction pattern from 180 °C to room temperature (18 °C). Diffuse scattering in the form of streaks along the $\langle 110 \rangle_{B2}$ directions is apparent in these average diffraction patterns. These streaks can be seen above 32 °C and appear to increase in intensity during cooling as the temperature approaches M_S. Between 32 and

30 °C, the appearance of superlattice peaks at the ½ $\{110\}_{B2}$ superlattice positions announce the arrival of the transformation front and indicate that the B19' martensite structure is beginning to form.

The B19' phase of NiTi takes the form of 12 lattice correspondent variants that lie on 4 unique crystallographic planes with the B2 parent phase owing to the cubic symmetry and are reported by Matsumoto et al. [38]. In our experiment, only 9 of the variants can be uniquely differentiated along the $[111]_{B2}$ zone axis (for more information refer to Fig. S1), and our field of view is typically within one habit plane. Here, it is only possible to identify three unique correspondent martensite variant types, by classifying them in terms of the plane on which the superlattice peak pairs appear. The diffraction patterns associated with each of these three unique variant types are superimposed and shown in Fig. 1a. The red, green, and blue colors correspond to each variant type and white peaks are present in diffraction from all three variants.

From the 4D-STEM diffraction patterns, the intensity of the superlattice peaks associated with each variant are then integrated and mapped as shown in Fig. 1c. From 180 °C to 33 °C no martensite structure is observed. At 32 °C, the transformation front becomes apparent as stripes of variants 1 and 3, appearing in the lower right of the scan area. At 30 °C the transformation front progresses through the majority of the field of view with only upper left scan area left untransformed. As the sample is cooled below 30 °C variant 2 appears in the upper left corner. By 28 °C the entire field of view is transformed martensite and is identical to the final structure visualized at 18 °C.

This phase mapping method clearly shows the martensite variants and progression of the transformation front. Recent advancements by Ophus et al. [31] makes it possible to perform high throughput indexing of electron diffraction patterns, thereby eliminating the need for any information outside the expected crystal structure. Using this method, the full 3D crystal orientation can be resolved. However, the orientation relationship between martensite and austenite structures in NiTi has been well studied [1] such that we can limit the indexable zone axes to $\{1\text{–}10\}_{B19'}$ when accounting for double diffraction. Using this known orientation relationship, the in-plane rotation of the martensite is mapped in Fig. 1d. This method also clearly demonstrates the progression of the transformation front.

Both the diffraction pattern indexing method and the direct integration of the B19' superlattice peaks assumes that only B19' martensite is present. These methods do not necessarily preclude the presence of the secondary intermediate martensite, the R-phase. However, the DSC curve shown in Fig. 2a shows a clear single peak for both the forward and reverse transformation indicating a one-step phase transformation. This is further corroborated by Fig. 2(b–g,k) which shows the maximal

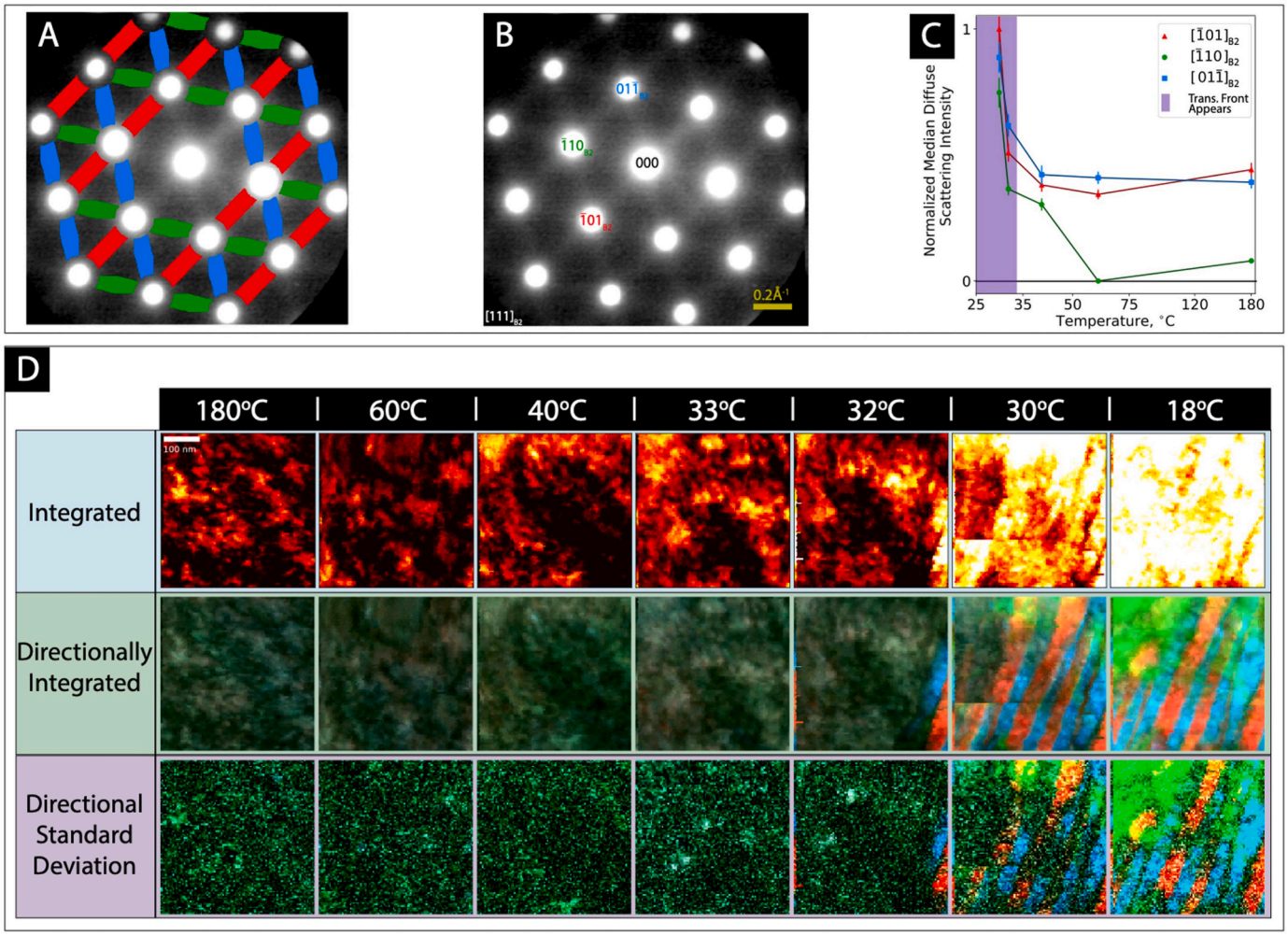

Fig. 3. Analysis of diffuse streaking before and through phase transformation. (a) Virtual detector areas overlaid on the average diffraction pattern at 33 °C indicating the regions and colors used to create images in (d); red, green, and blue indicate streaking direction associated with each individual variant used to produce the coloration of each image in (d), the average diffraction pattern at 33 °C (b) showing clear diffuse streaking along the $\langle 110\rangle_{B2}$, (c) the diffuse streaking intensity between B2 parent peaks along each lattice direction indicated in (c), (d) the integrated value, directionally integrated value, and directional standard deviation of the detector areas mapped during sample cooling from 180 °C to 18 °C. (For interpretation of the references to color in this figure legend, the reader is referred to the Web version of this article.)

diffraction pattern from the 4D-STEM scan acquired at the temperature indicated. Each 4D-STEM data set in this experiment contains 10,000 individual diffraction patterns. The maximal diffraction pattern is calculated by taking the maximum value for each pixel in diffraction space across all 10,000 patterns. This calculation is highly sensitive to changes in diffraction peaks, even if they are present in only a single pattern. Simulated electron diffraction patterns for the B2, B19', and R phases are shown in Fig. 2h-j. There are no apparent R-phase peaks present in the maximal diffraction patterns either before, during, or after the B19' transformation front has passed through the field of view. It is worth noting the temperature discrepancy between the DSC measurement (M_s of ~55 °C) and the *in situ* 4D-STEM measurement (M_s of 32 °C). This difference in the electron-transparent TEM sample is attributed to the well-known thin film effect in NiTi which suppresses M_s as the B2→B19' phase transition is slightly more difficult to induce in thin samples [39,40] owing to surface effects.

3.2. Diffuse streaking and strain in pre-transitional NiTi

The diffuse scattering in the form of streaking is illustrated in Fig. 3, where we consider the potential formation of the martensite variants rather than R-phase formation. Fig. 3a shows the colored area of the patterns used to measure the diffuse streaking overlaid on the average diffraction pattern at 33 °C. Each color indicates the streaking along a direction associated with one of the three variants that are formed. Notably, the first order streaks were not included in these virtual detectors. This was done to eliminate inelastic scattering contributions which are concentrated near the center disk. Three values were extracted from these detector areas: median value, integrated value, and standard deviation. These three values were chosen to differentiate the true streaking as opposed to martensite reflections where the median is used to determine the skew of the intensity values within each detector area. The standard deviation is calculated to determine if the pixel intensities in the detector are highly dispersed. Data that is highly dispersed and skewed is likely to suggest martensite peaks as opposed to diffuse streaks. This is apparent as the martensite variants which form from 32 °C to 18 °C are clearly visible in the standard deviation maps.

Diffuse streaking is clearly present ahead of the transformation front, however, the *in situ* 4D-STEM mapping on cooling in Fig. 3 do not show any directional preference for such streaks. The directional standard deviation, similarly, does not indicate martensite nucleation ahead of the transformation front. While there does not seem to be any discernible spatial structural variation in the diffuse streaking within the length scale studied here, there is a notable shift in the intensity of the diffuse streaking with changing temperature as depicted in Fig. 3c.

The temperature dependence observed in this experiment has been previously reported in this composition space [1,25,41] and is closely associated with the pre-transitional state of materials which undergo displacive phase transformations [19]. Fig. 3c shows the change in diffuse scattering intensity with respect to temperature. During cooling, a notable increase is seen at about 40 °C directly preceding the transformation front. For this calculation, all areas of each scan containing martensite reflections were removed using masks as illustrated in Fig. S2 where streaking along the $[001]_{B19'}$ direction for all three variants is mapped, suggesting the same trend upon cooling. Fig. 4a shows a complementary measure of the average lattice strain along the B2 directions linked to each of the martensite variants that are formed during the cooling process. The strain was measured relative to the B2 lattice vectors identified at 180 °C. As expected, the lattice exhibits contraction upon cooling that is consistent with reported coefficient of thermal expansion [42,43] for B2 NiTi. Significant changes in strain along all three directions become evident as the transformation front approaches, beginning at 32 °C. The strain shows apparent correlation to the diffuse scattering intensity measured at each temperature and is consistent with trends identified in Fig. 4a and 3c. The lattice strain is mapped in Fig. 5 to visualize the strain distribution over the sample area and to further investigate any correlation between diffuse streaking and strain.

Fig. 5a shows the diffraction pattern with the superlattice peaks from each of the three variants colored red, blue, and green. Fig. 5(b–e) demonstrates the transformation front progression between 33 °C and 18 °C that each martensite variant is tracked by direct integration of the superlattice peak locations from 4D-STEM. Fig. 5f-i maps the strain landscape at the nanoscale across the sample along the $[-101]_{B2}$ direction (gray dashed arrow in Fig. 5a). The relative strain at each temperature is measured with respect to the median B2 lattice (assuming zero net strain) over the entire scan area. Moreover, there are no clear strain heterogeneities within the B2 phase directly preceding the phase transition.

Once the monoclinic martensite variants have formed via shrinking of the relevant $\langle 100\rangle_{B2}$ and $\langle 011\rangle_{B2}$ lattice direction, to form the martensite a- and b-axes. Moreover, the relevant $\langle 011\rangle_{B2}$ direction expands to form the c-axis, and finally shears along the relevant $\langle 100\rangle_{B2}$ direction to form the monoclinic angle, thereby dramatically changing the strain landscape. The expansion of the B2 lattice along the strain axis

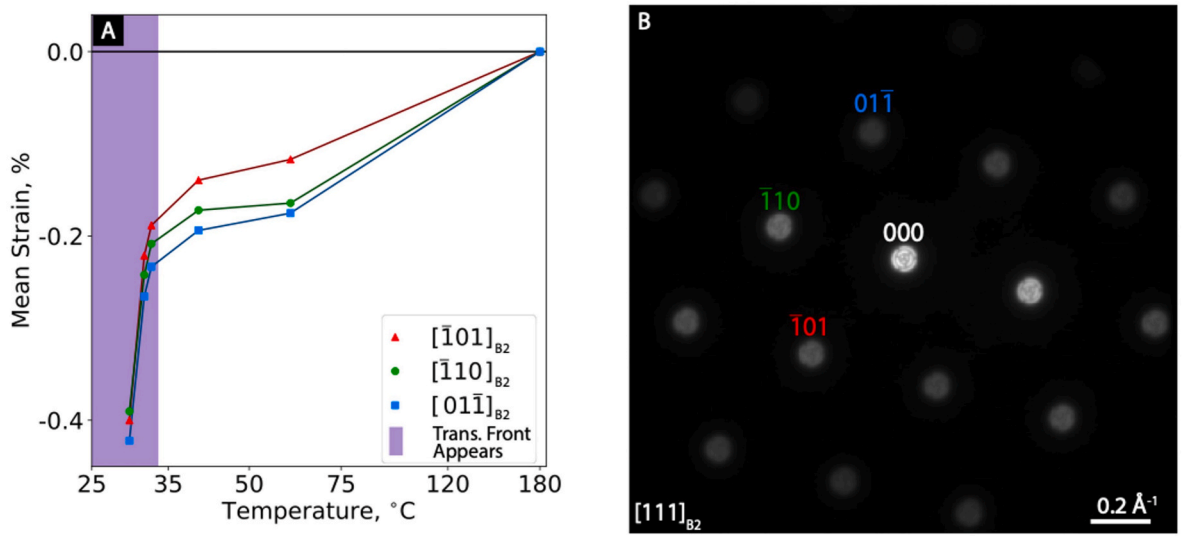

Fig. 4. Strain analysis of the 3 variant directions in austenite through the phase transformation (a) thermal evolution during cooling of B2 austenite lattice strain of along the noted directions associated with each martensite variant as indicated in (b) the indexed average diffraction pattern at 33 °C.

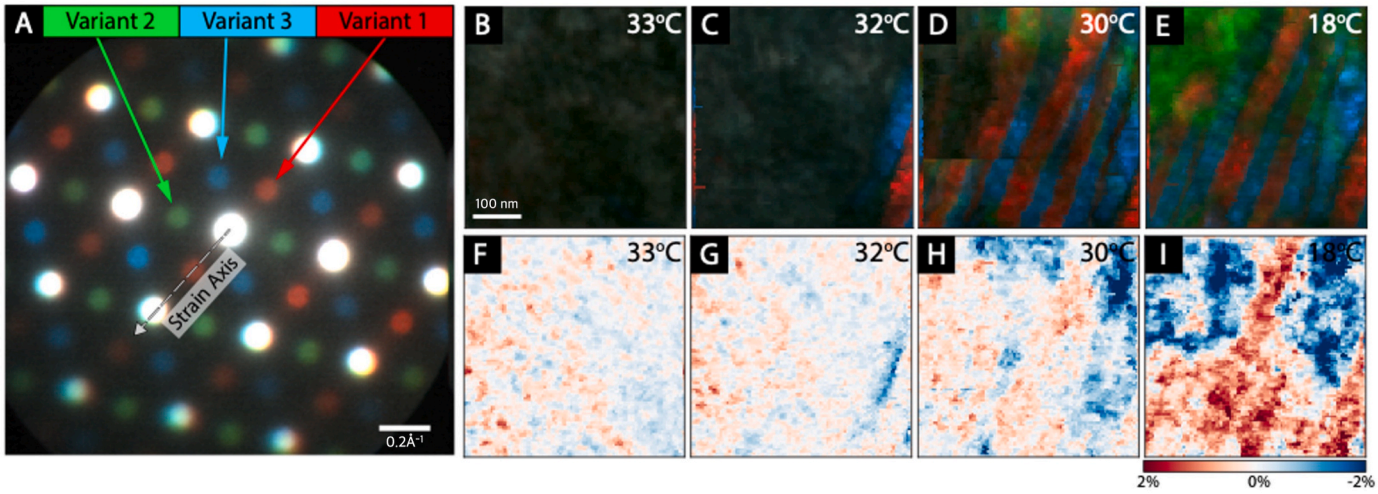

Fig. 5. Strain in pre-transitional austenite. (a) average diffraction pattern at 18 °C demonstrating color-coded superlattice Bragg peaks associated with the three martensite variants which form on cooling as demonstrated in (b–e) which show the formation of the B19' martensite structure in NiTi during cooling and (f–i) the corresponding lattice strain maps measured along the lattice direction indicated in (a). Note: (f–i) strain is measured relative to the median strain at a given temperature. (For interpretation of the references to color in this figure legend, the reader is referred to the Web version of this article.)

to form the $[001]_{M1,B19'}$ direction leads to a large strain associated with variant 1. Variants 2 and 3 demonstrate a reduced strain due to the shrinking of the B2 lattice along the strain axis associated with the formation of the a- and b-axes for these variants. This strain mapping method elucidates the real space transformation dynamics in NiTi at the nanoscale and agrees well with previously reported theory [44] on the lattice correspondence between the cubic B2 and monoclinic B19' phases in NiTi. Importantly, it also provides insight into the nanoscale

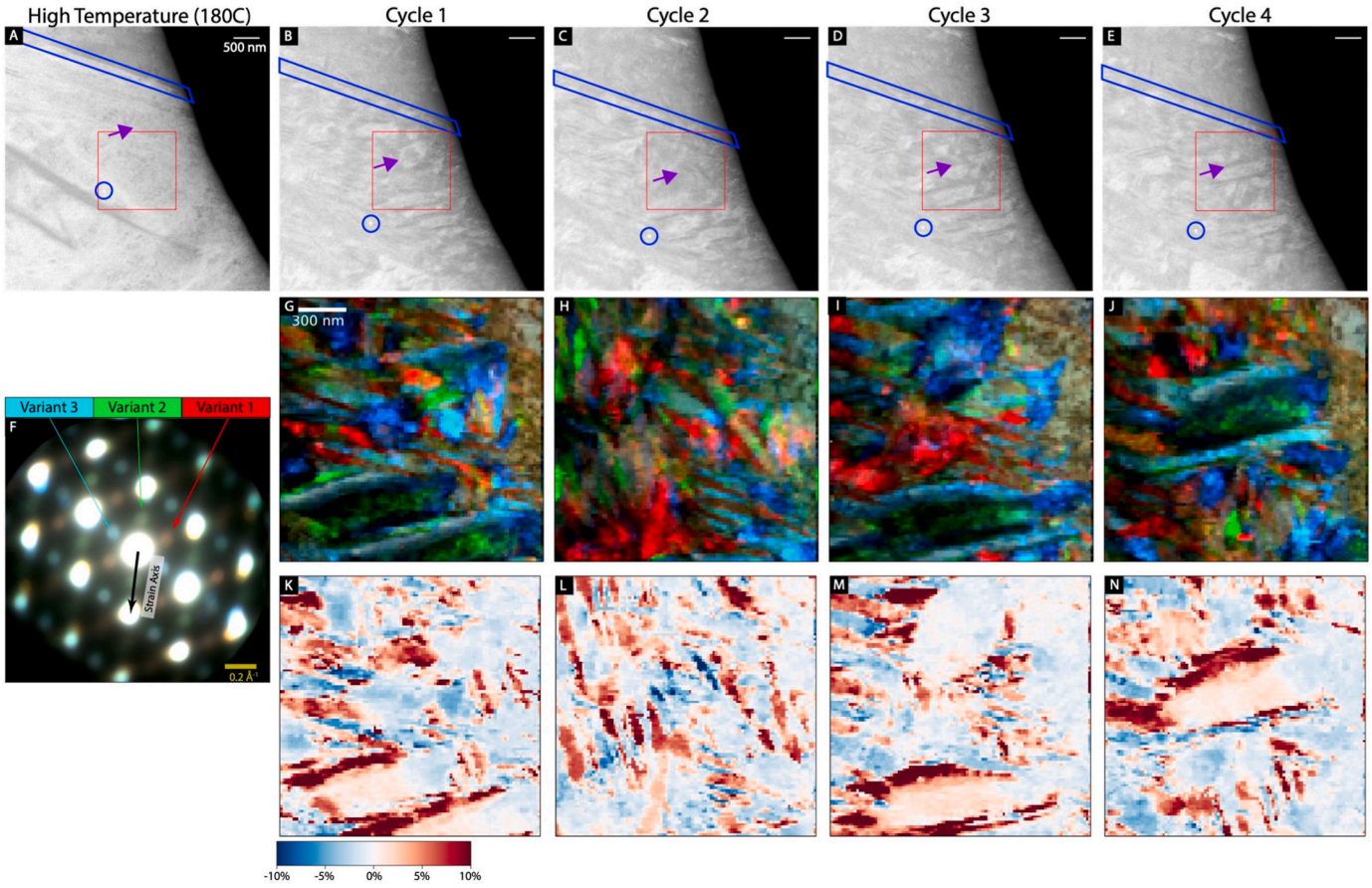

Fig. 6. Cyclic variation in martensite structure. (a) ADF-STEM image of B2 austenite NiTi at 180 °C with blue markers indicating static fiducial markers in the form of a linear grain boundary and an electron beam deposited carbon contamination spot, (b–e) ADF images of the formed martensite structure in NiTi at room temperature after each thermal cycle, (g–j) 4D-STEM images taken from the highlighted areas in (b–e) showing the distribution of three martensite variants as identified by the corresponding superlattice peaks marked in the diffraction pattern (f), and (k–n) corresponding 4D-STEM strain maps along the direction indicated in (f). (For interpretation of the references to color in this figure legend, the reader is referred to the Web version of this article.)

B2 strain landscape directly preceding the phase transition.

3.3. Evolution of martensitic structure on thermal cycling in NiTi

Up to this point, we have described only the formation of the martensite structure from the austenite phase in response to cooling through the transition temperature. However, whether or how the martensite structure evolves via thermal cycling is an open question. While previous reporting [15] suggests that the martensite would form the same structure repeatedly, more recent findings [16–18] indicate the morphology of the martensite lath structure varies with increasing number of thermal cycles. Therefore, the following section details an experiment where a NiTi sample was thermally cycled *in situ* four times and examined with 4D-STEM to address whether the structure varies on cycling and elucidate the nature of this possible variation.

Fig. 6a shows the fully austenitic NiTi sample before the first cycle. Fig. 6b-e show the resulting martensitic structure after thermal cycling. Blue arrows indicate features that are used as fiducial markers in all images. The purple arrow in Fig. 6e highlights a clearly distinguishable martensitic feature. This feature appears to shift in location through subsequent cycles as shown in Fig. 6b-d.

Following initial observations in image contrast through Annular Dark Field (ADF)-STEM, complimentary 4D-STEM scans were taken to understand the structural changes after each thermal cycle over approximately the same sample area. The 4D-STEM martensite variant maps shown in Fig. 6g-j were acquired from the pink highlighted areas in corresponding ADF-STEM images in Fig. 6b-e. These variant maps clearly illustrate a martensitic lath structure that varies upon cycling. Critically, the scans do not demonstrate the same distribution of habit plane variants. A common feature was identified in all scans Fig. 6b, d-e where one large stripe of variant 2 is encapsulated by two large stripes of variant 3 (blue-green-blue horizontal feature located in the center of Fig. 6j). This feature is missing in Fig. 6h, however, there is a similar feature visible in the corresponding ADF-STEM image directly below the scan area. This evidence suggests the feature may have been present in cycle 2 and simply not located within the 4D-STEM area. Several similar features are observed across the four cycles, indicating that while the exact martensitic structure is not recreated in each cycle, there exists considerable similarity in the structures that do form. This is further evidenced in the strain maps shown in Fig. 6k-n which show the strain along the c-axis of variant 2. These strain maps provide a potentially clearer depiction of the distribution of variant 2 and highlight the presence of similar martensitic structures, including their directionality and size.

In summary, it can be seen that NiTi does not consistently adopt the same exact B19' martensite structure when cycled through the B2→B19' phase transition. However, there is considerable similarity in the martensitic structures that do form upon thermal cycling.

4. Discussion

4.1. The structure in B19' martensite

Fig. 1 directly demonstrates the progression of the B2→B19' transformation front in NiTi showing the formation of three martensite variants. To truly understand the structure of these variants, it is critical to bear in mind that B19' martensite can yield 12 lattice correspondence variants owing to the cubic symmetry of the B2 phase. However, while 12 correspondence variants are possible, the current mode of martensite variant mapping (Fig. 1) reveals only three variant classes, each containing four martensite correspondence variants.

To understand this, we delve briefly into the crystallography of the B2/B19' lattice correspondence. Using the lattice correspondence matrix reported by Otsuka and Ren [1], four unique B19' zone axes can be derived which correspond to the $[111]_{B2}$ zone. Simulated diffraction patterns for each of these B19' zone axes are shown in Fig. S1. Each B19' diffraction pattern exhibits two-fold symmetry while the $[111]_{B2}$ exhibits six-fold symmetry. This implies that each of the four B19' zone axes can have three unique in-plane rotations to account for all 12 correspondence variants.

Nonetheless, due to the necessity for a certain sample thickness to avoid suppressing the martensitic transformation, the convergence angle required to obtain a small electron probe, and the inherent lack of information about crystal symmetry along the beam direction, the initial 12 unique correspondence variants are effectively consolidated to three diffraction patterns which can be distinguished by integrating the superlattice peaks, as illustrated in Fig. 1. For more in-depth discussion, please refer to Fig. S1 and subsequent discussion in the supplemental information.

The failure of this integration method to differentiate all 12 correspondence variants is largely owed to the insensitivity to small changes in peak locations. The four martensite zone axes present in Fig. S1 clearly demonstrate unique strain states with respect to the original parent lattice. $[101]_{B19'}$ shows lattice expansion, while $[-101]_{B19'}$ expresses contraction, and lattice shear along $[-110]_{B19'}$, and $[110]_{B19'}$, respectively. This variation in strain state is more clearly demonstrated in the peak splitting observed in the purple inset of Fig. 7b. Peak splitting is emphasized with the overlaid 2D lattices shown in the yellow inset of Fig. 7b. When viewed along the $[110]_{B19'}$ zone axis (Fig. S1), it is apparent that variant 1 and 3 exhibit lattice shearing. In contrast, variant 2 displays a lattice contraction, characterized by increased peak spacing, indicating an orientation with $[-101]_{B19'}$ alignment.

To reinforce this observation, we assess the strain state of the lattice, as shown in Fig. 7d-f. This figure displays ε_{xx}, $\varepsilon_{xy,}$ and ε_{yy} with respect to the axes indicated in Fig. 7b. Variant 2 exhibits a negative strain state in all directions which agrees well with the simulated $[-101]_{B19'}$ diffraction. Conversely variant 1 shows negative ε_{xx}, and ε_{xy} but positive ε_{yy} which agrees well with the simulated $[-110]_{B19'}$ diffraction. Variant 3 expresses exactly the opposite trend to variant 1 indicating a $[-110]_{B19'}$ with a different in-plane rotation. This shows that, while integrating superlattice peaks can only differentiate three martensite variant structures, the combination of careful calibration and strain analysis enables *in situ* 4D-STEM to distinguish up to 9 correspondence variants. 4D-STEM from an additional complementary zone axis would be required to distinguish the remaining three variants.

By discerning the orientation of the three variants through the strain state, we gain a clearer understanding of the martensite morphology and the distribution of variants that develop. Fig. 7a contains alternating stripes of variant 1 and variant 3, while variant 2 shows a more isotropic morphology. The alternating stripes of variants 1 and 3 are a twin structure which suggests a type I $\{111\}_{B19'}$ twin is present (shown schematically in Fig. 7h). This was ascertained by indexing the respective diffraction patterns as shown in Fig. 7c. These transformation twins are well known to form as a way to accommodate for the lattice mismatch between the austenite and martensite phases. The type II $\langle 011\rangle_{B19'}$ twinning mode has been observed to be the most dominant twinning mode in NiTi, however expected type I {111} twins are also present [1].

Variants 1 and 3, whose boundaries are indicated by the change in red and blue colors in Fig. 7a, exhibit opposite strains as is emphasized by the change between positive (red) and negative (blue) at similar magnitudes as shown indicated by Fig. 7d-f. This demonstrates a way to directly visualize the strain accommodation in the martensite lattice that is afforded by the twins to account for the volumetric difference between the martensite and austenite phases. Some of the variants overlap, which is a consequence of the sample thickness being slightly larger than of the average lath width.

4.2. Origin of diffuse streaking and predictive structures in pre-transitional NiTi

Having addressed the martensitic structure which develops on

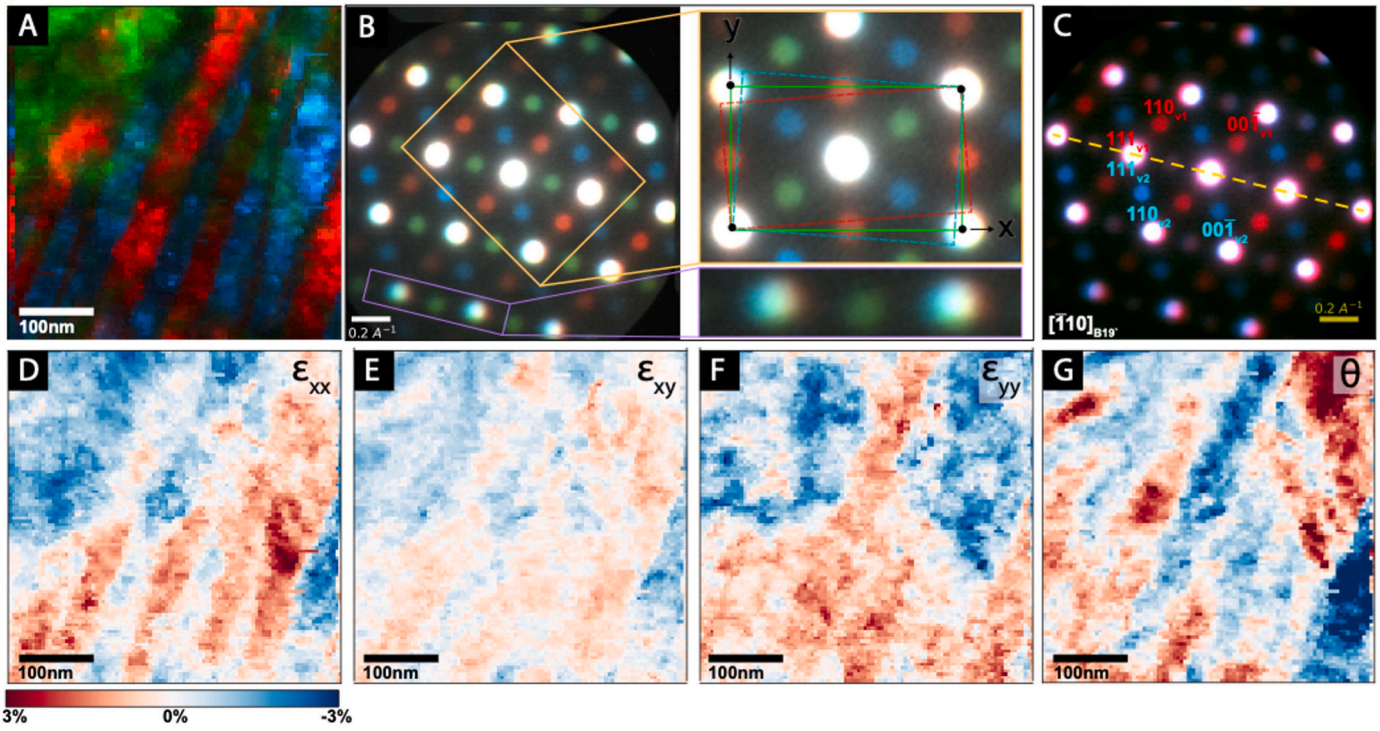

Fig. 7. Twinning and self accommodation. (a) Martensite phases mapped at 18 °C, (b) average diffraction pattern with red, green, and blue channels corresponding to the martensite variants in (a), orange zoom-ins shows lattice shear associated with each variant, and purple zoom-in shows the peak splitting associated with the shear and contraction of the variants, (c) the indexed diffraction from variants 1 and 3 demonstrating twin nature (yellow line indicates twinning plane) and (d–g) ε_{xx}, ε_{xy}, ε_{yy}, and lattice rotation, θ, respectively (x- and y-axes are indicated in orange zoom-in in (b)). (For interpretation of the references to color in this figure legend, the reader is referred to the Web version of this article.)

cooling, we now focus on the development of the austenitic structure directly preceding the phase transformation. Fig. 1 contains diffuse streaks along the $[110]_{B2}$ in the austenite phase at temperatures above M_s (~33°C). Fig. 2b-g,k identify no intermediate martensite phases and Fig. 2a confirms this by demonstrating a one-step phase transformation. Therefore, one may conclude that the diffuse streaking observed here does not originate from Bragg scattering of an intermediate phase.

Fig. 8 shows the average diffraction patterns of the untransformed area, the transformed area and at the transformation front. The diffuse streaking at the transformation front remains relatively stable, while the untransformed material consistently exhibits clear diffuse streaking. This shows that the diffuse streaking does not originate from a bulk averaging effect of the newly transformed martensite at the transformation front. Moreover, the diffuse streaking observed here is likely a true symptom of the pre-transitional state in the B2 austenite phase.

Previously reported explanations for pre-transitional anomalies, such as diffuse streaking, can be classified into two categories: static heterogeneities and long-range effects. Static heterogeneities include explanations like residual martensite, chemical segregation, and structural defects, while long-range effects include uniform lattice strain, phonon softening, and general thermodynamic phase instability [1]. Fig. 3 shows a homogeneous distribution of diffuse streaking and Fig. 8 confirms that no interfacial localization is observed, both of which suggest the origin of this diffuse streaking is a long-range phenomenon rather than a static heterogeneity.

While there is an apparent correlation between evolution of strain and diffuse streaking intensity as the temperature approaches M_s, it is unlikely that the strain is responsible for the development of such pronounced diffuse streaks. Rather, it is likely that the strain is influenced by both thermal contraction and the instability of the austenite phase with respect to the emerging martensite phase. Therefore, the origin of the diffuse streaking observed in pre-transitional B2 NiTi is not likely caused by static heterogeneities or the strain landscape.

Additionally, *in situ* 4D-STEM allows for observation of the directionality of strain and streaking in the pre-transitional austenite phase. Figs. 3–5 demonstrate no clear preferential directionality which would provide insight into the subsequent formation of a specific martensite variant or the factors governing one variant forming over another. The strain landscape and diffuse streaking both appear homogeneous and isotropic with respect to the $\langle 110 \rangle_{B2}$ directions. Previous findings[6] suggest that diffuse streaking indicates the pre-transitional austenite phase may hold information about the martensite structure to come, however our findings suggest this is not the case.

4.3. Cyclic variation of martensite on thermal cycling

Fig. 6 shows the evolution of the martensite structure in NiTi on thermal cycling as visualized through 4D-STEM structure mapping and ADF-STEM. It is observed that NiTi does not form the same B19' martensite lath structure on repeated thermal cycling through the B2→B19' phase transition, however, it does appear to retain similar qualities in subsequent cycles.

It is well understood that martensitic transformations are associated with localized lattice strains which assist in producing dislocations in a phenomenon known as transformation-induced plasticity. Miyazaki et al. [45] and Simon et al. [46] have clearly shown the transformation-induced dislocations and increase in dislocation density on thermal cycling in NiTi. These transformation-induced dislocations, depending on their burgers-vector, can either inhibit [45] or promote martensite formation [46,47]. In some cases, they can also act as martensite nucleation sites [48]. These dislocations have been theorized to account for the observed variation in martensite structure on repeated cycling.

The similarity of the martensitic structure on cycling is likely due to the plethora of nucleation sites available in this polycrystalline NiTi. Preferential heterogenous nucleation at these sites allows the

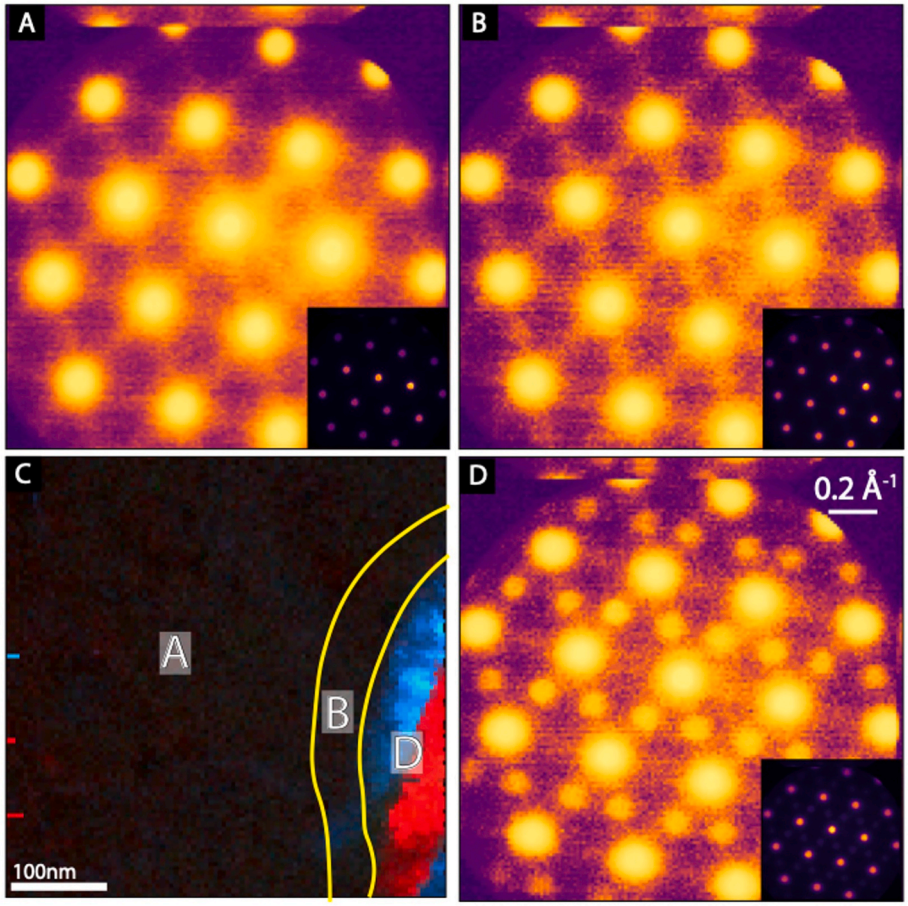

Fig. 8. Diffraction patterns across the transition front mapped at 32°C. (a) average diffraction pattern (contrast adjusted to show diffuse streaking) from the area hundreds of nanometers away from the transition front (b) average diffraction pattern (contrast adjusted to show diffuse streaking) within the region less than 100 nm away from the transition front (c) the different areas mapped at 32 °C with three regions representing the austenite phase, the transformation front, and the transformed area corresponding to the diffraction patterns and (d) average diffraction pattern from the transformed region. (a,b,d) shown with inset diffraction pattern showing linear scaling over the whole intensity range.

transformation fronts to progress in the same manner on during each cycle. Fig. S3 demonstrates the heterogenous nucleation of martensite at precipitate boundaries and the resulting progression of the transformation front. This clearly demonstrates the importance of nucleation sites in determining the final martensite structure. However, when the transformation front encounters dislocations induced during cycling after nucleation, it undergoes slight variations, resulting in a martensite lath structure that is similar to previous iterations yet exhibits some variability.

5. Conclusions

In this study, it is demonstrated that *in situ* 4D-STEM is an effective technique to map the structural evolution of the martensitic phase transformation in NiTi at high spatial resolution. 4D-STEM imaging shows that the distribution of martensite correspondence variants reveals the development of type I $\{-111\}_{B19'}$ twins and directly visualizes, through the nanoscale strain landscape, the self-accommodation mechanism in B19' martensite.

Mapping of the pre-transitional diffuse streaking shows a uniformity preceding the B2→B19' transformation front and no localization is observed indicating the origin is likely a long-range homogenous phenomenon. There is no preferential directionality of diffuse streaks or strain in the pre-transitional B2 lattice, and no structures are observed to be predictive of the coming martensite structure.

Finally, NiTi exposed to multiple B2→B19' thermal transformation cycles reveals a varied martensitic structure that in some ways is connected to the prior cycle. These variations are connected to accumulating transformation-induced dislocations while the similarities between cycles likely originates from the large-scale heterogeneous nucleation sites available in this polycrystalline sample.

This novel application of a modern characterization technique (4D-STEM) to the well-studied problem of the NiTi martensitic phase transformation demonstrates the power of nanoscale structural mapping as a tool for studying the progression of the phase transformation fronts in NiTi by directly imaging the pre-transitional state and the evolution of martensitic lath structure via thermal cycling.

CRediT authorship contribution statement

Jennifer Donohue: Writing – review & editing, Writing – original draft, Methodology, Formal analysis, Data curation, Conceptualization. **Sean H. Mills:** Writing – review & editing, Methodology, Data curation, Conceptualization. **Benjamin H. Savitzky:** Software. **Steven E. Zeltmann:** Data curation. **Colin Ophus:** Software, Methodology. **Andrew M. Minor:** Writing – review & editing, Writing – original draft, Supervision, Project administration, Methodology, Funding acquisition, Conceptualization.

Declaration of competing interest

The authors declare they have no competing interests, financial or

otherwise for the following paper:

Acknowledgements

This work was supported by STROBE: A National Science Foundation Science and Technology Center under Grant No. DMR 1548924. JD was supported by the Department of Defense (DoD) through the National Defense Science and Engineering Graduate (NDSEG) Fellowship Program. SM was supported by FUTURE (Fundamental Understanding of Transport Under Reactor Extremes), an Energy Frontier Research Center funded by the U.S. Department of Energy, Office of Science, Basic Energy Sciences. BS was supported by the Toyota Research Institute. Work at the Molecular Foundry at Lawrence Berkeley National Laboratory was supported by the U.S. Department of Energy under Contract # DE-AC02-05CH11231.

Appendix A. Supplementary data

Supplementary data to this article can be found online at https://doi.org/10.1016/j.msea.2025.147951.

Data availability

Data will be made upon reasonable request to the corresponding author.

References

[1] K. Otsuka, X. Ren, Prog. Mater. Sci. 50 (2005) 511–678.
[2] J. Katsuyama, T. Kobayashi, P. Chalermkarnnon, M. Mizuno, H. Araki, Y. Shirai, Mater. Trans. 43 (2002) 1489–1493.
[3] E. Polatidis, M. Šmíd, I. Kuběna, W.-N. Hsu, G. Laplanche, H. Van Swygenhoven, Mater. Des. 191 (2020) 108622.
[4] T.W. Duerig, A. Pelton, D. Stöckel, Mater. Sci. Eng., A 273 (1999) 149–160.
[5] Y. Furuya, H. Shimada, Mater. Des. 12 (1991) 21–28.
[6] M. Nishida, T. Nishiura, H. Kawano, T. Inamura, Phil. Mag. 92 (2012) 2215–2233.
[7] W.J. Buehler, J.V. Gilfrich, R.C. Wiley, J. Appl. Phys. 34 (1963) 1475–1477.
[8] A. Foroozmehr, A. Kermanpur, F. Ashrafizadeh, Y. Kabiri, Mater. Sci. Eng., A 528 (2011) 7952–7955.
[9] J. Ye, R.K. Mishra, A.R. Pelton, A.M. Minor, Acta Mater. 58 (2010) 490–498.
[10] C. Wayman, I. Cornelis, K. Shimizu, Scripta Metall. 6 (1972) 115–122.
[11] C. Maletta, E. Sgambitterra, F. Furgiuele, R. Casati, A. Tuissi, Int. J. Fatig. 66 (2014) 78–85.
[12] Y. Wu, E. Ertekin, H. Sehitoglu, Acta Mater. 135 (2017) 158–176.
[13] R.F. Hamilton, H. Sehitoglu, Y. Chumlyakov, H.J. Maier, Acta Mater. 52 (2004) 3383–3402.
[14] J. Hurley, A.M. Ortega, J. Lechniak, K. Gall, H.J. Maier, Int. J. Mater. Res. 94 (2022) 547–552.
[15] K. Otsuka, T. Sawamura, K. Shimizu, C. Wayman, Metall. Trans. A 2 (1971) 2583–2588.
[16] R. Basu, L. Jain, B. Maji, M. Krishnan, K. Mani Krishna, I. Samajdar, P. Pant, Metall. Mater. Trans. 43 (2012) 1277–1287.
[17] A. Churakova, D.V. Gunderov, Metals 10 (2020) 227.
[18] A. Sibirev, E. Ubyivovk, S. Belyaev, N. Resnina, Mater. Lett. 319 (2022) 132267.
[19] Y.M. Jin, Y.U. Wang, Y. Ren, npj Comput. Mater. 1 (2015) 1–14.
[20] Y.-C. Xu, W.-F. Rao, J.W. Morris Jr., A.G. Khachaturyan, npj Comput. Mater. 4 (2018) 58.
[21] X. Ren, N. Miura, K. Taniwaki, K. Otsuka, T. Suzuki, K. Tanaka, Y.I. Chumlyakov, M. Asai, Mater. Sci. Eng., A 273 (1999) 190–194.
[22] X. Ren, K. Taniwaki, K. Otsuka, T. Suzuki, K. Tanaka, Y.I. Chumlyakov, T. Ueki, Philos. Mag. A 79 (1999) 31–41.
[23] J. Zhang, X. Ren, K. Otsuka, K. Tanaka, Y.I. Chumlyakov, M. Asai, Materials transactions, JIM 40 (1999) 385–388.
[24] X. Ren, N. Miura, J. Zhang, K. Otsuka, K. Tanaka, M. Koiwa, T. Suzuki, Y. I. Chumlyakov, M. Asai, Mater. Sci. Eng., A 312 (2001) 196–206.
[25] Q. Liang, D. Wang, J. Zhang, Y. Ji, X. Ding, Y. Wang, X. Ren, Y. Wang, Phys. Rev. Mater. 1 (2017) 033608.
[26] X. Ren, K. Otsuka, T. Suzuki, J. Alloys Compd. 355 (2003) 196–200.
[27] H. Sehitoglu, R. Anderson, I. Karaman, K. Gall, Y. Chumlyakov, Mater. Sci. Eng., A 314 (2001) 67–74.
[28] P. Hua, K. Chu, F. Ren, Q. Sun, Acta Mater. 185 (2020) 507–517.
[29] H. Tietze, M. Mullner, B. Renker, J. Phys. C Solid State Phys. 17 (1984) L529.
[30] B.H. Savitzky, S.E. Zeltmann, L.A. Hughes, H.G. Brown, S. Zhao, P.M. Pelz, T. C. Pekin, E.S. Barnard, J. Donohue, L.R. DaCosta, others, Microsc. Microanal. 27 (2021) 712–743.
[31] C. Ophus, S.E. Zeltmann, A. Bruefach, A. Rakowski, B.H. Savitzky, A.M. Minor, M. C. Scott, Microsc. Microanal. 28 (2022) 390–403.
[32] C. Ophus, Microsc. Microanal. 25 (2019) 563–582.
[33] S. Pourbabak, A. Orekhov, D. Schryvers, Microsc. Res. Tech. 84 (2021) 298–304.
[34] S.E. Zeltmann, A. Müller, K.C. Bustillo, B. Savitzky, L. Hughes, A.M. Minor, C. Ophus, Ultramicroscopy 209 (2020) 112890.
[35] Y. Kudoh, M. Tokonami, S. Miyazaki, K. Otsuka, Acta Metall. 33 (1985) 2049–2056.
[36] T. Hara, T. Ohba, E. Okunishi, K. Otsuka, Materials transactions, JIM 38 (1997) 11–17.
[37] K. Parlinski, M. Parlinska-Wojtan, Phys. Rev. B 66 (2002) 064307.
[38] O. Matsumoto, S. Miyazaki, K. Otsuka, H. Tamura, Acta Metall. 35 (1987) 2137–2144.
[39] S. Mao, H. Li, Y. Liu, Q. Deng, L. Wang, Y. Zhang, Z. Zhang, X. Han, J. Alloys Compd. 579 (2013) 100–111.
[40] H. Li, S. Mao, K. Zang, Y. Liu, Z. Guo, S. Wang, Y. Zhang, X. Yin, J. Alloys Compd. 588 (2014) 337–342.
[41] D. Wang, Z. Zhang, J. Zhang, Y. Zhou, Y. Wang, X. Ding, Y. Wang, X. Ren, Acta Mater. 58 (2010) 6206–6215.
[42] J.B. Haskins, J.W. Lawson, J. Appl. Phys. 121 (2017).
[43] S. Qiu, U. Central Florida, Electronic Theses and Dissertations, 2010.
[44] S. Miyazaki, S. Kimura, K. Otsuka, Y. Suzuki, Scripta Metall. 18 (1984) 883–888.
[45] S. Miyazaki, Y. Igo, K. Otsuka, Acta Metall. 34 (1986) 2045–2051.
[46] T. Simon, A. Kröger, C. Somsen, A. Dlouhy, G. Eggeler, Acta Mater. 58 (2010) 1850–1860.
[47] A. Yawny, M. Sade, G. Eggeler, Int. J. Mater. Res. 96 (2022) 608–618.
[48] T. Fukuda, T. Saburi, K. Doi, S. Nenno, Materials Transactions, JIM 33 (1992) 271–277.